Structural controls on the formation of BSR over a diapiric anticline from a dense MCS survey offshore southwestern Taiwan

Philippe Schnürle [a],*, Char-Shine Liu [b], Andrew T. Lin [c], Saulwood Lin [b]

[a] Institute of Marine Geosciences, Ifremer, 29280 Brest, France
[b] Institute of Oceanography, National Taiwan University, Taipei, Taiwan, ROC
[c] Institute of Geophysics, National Central University, Jungli, Taiwan, ROC

ARTICLE INFO

ABSTRACT

A dense seismic reflection survey with up to 250-m line-spacing has been conducted in a 15 × 15 km wide area offshore southwestern Taiwan where Bottom Simulating Reflector is highly concentrated and geochemical signals for the presence of gas hydrate are strong. A complex interplay between north–south trending thrust faults and northwest–southeast oblique ramps exists in this region, leading to the formation of 3 plunging anticlines arranged in a relay pattern. Landward in the slope basin, a north–south trending diapiric fold, accompanied by bright reflections and numerous diffractions on the seismic profiles, extends across the entire survey area. This fold is bounded to the west by a minor east-verging back-thrust and assumes a symmetric shape, except at the northern and southern edges of this area, where it actively overrides the anticlines along a west-verging thrust, forming a duplex structure. A clear BSR is observed along 67% of the acquired profiles. The BSR is almost continuous in the slope basin but poorly imaged near the crest of the anticlines. Local geothermal gradient values estimated from BSR sub-bottom depths are low along the western limb and crest of the anticlines ranging from 40 to 50 °C/km, increase toward 50–60 °C/km in the slope basin and 55–65 °C/km along the diapiric fold, and reach maximum values of 70 °C/km at the southern tip of the Good Weather Ridge. Furthermore, the local dips of BSR and sedimentary strata that crosscut the BSR at intersections of any 2 seismic profiles have been computed. The stratigraphic dips indicated a dominant east–west shortening in the study area, but strata near the crest of the plunging anticlines generally strike to southwest almost perpendicular to the direction of plate convergence. The intensity of the estimated bedding-guided fluid and gas flux into the hydrate stability zone is weaker than 2 in the slope basin and the south-central half of the diapiric fold, increases to 7 in the northern half of the diapiric fold and plunging anticlines, and reaches a maximum of 16 at the western frontal thrust system. Rapid sedimentation, active tectonics and fluid migration paths with significant dissolved gas content impact on the mechanism for BSR formation and gas hydrate accumulation. As we begin to integrate the results from these studies, we are able to outline the regional variations, and discuss the importance of structural controls in the mechanisms leading to the gas hydrate emplacements.

1. Introduction

Widely distributed Bottom Simulating Reflector (BSR) was first identified offshore southwestern Taiwan more than a decade ago (Reed et al., 1992). Several studies dedicated to the distribution and the characteristics of the BSR in this region followed (e.g. Chi et al., 1998; Liu et al., 1997; Schnurle et al., 1999). In early 2004, the Central Geological Survey of Taiwan has initiated a gas hydrate field

investigation program with the objectives to map the regional gas hydrate distribution offshore SW Taiwan and to understand the geological, geophysical and geochemical characteristics of hydrate-bearing strata. Geophysical investigations performed include multichannel seismic (MCS) reflection and OBS wide-angle surveys, geothermal gradient measurements, deep-toed marine chirp and magnetic as well as toe-cam surveys. Geological and geochemical analyses of bottom water and core sediments are also performed. A suite of NW–SE trending multichannel seismic reflection profiles with a line-spacing of 1.8 km, that covers an area of 4800 km^2 offshore SW Taiwan in water depths ranging from 500 to 3500 m, revealed high concentration of BSR in tectonic settings from both

* Corresponding author.
E-mail address: philippe.schnurle@ifremer.fr (P. Schnürle).

the Manila accretionary prism and the passive margin of the South China Sea continental slope (Liu et al., 2006; Lin et al., 2009).

Dense marine seismic surveys related to hydrate exploration are scars; areas of conventional oil and gas interest are often covered by 3-dimensional seismic: the JIP in the Gulf of Mexico (e.g. Dai et al., 2008), the Norwegian offshore (e.g. Bünz et al., 2003; Hustoft et al., 2007), MITRI's hydrate exploration in Japan (e.g. Nagakubo et al., 2007), and Gulf of Guinea (e.g. Sultan et al., 2007) are notorious. Dense surveys conducted by academia are few: these include the vicinity of IODP drilling sites, for instance on the Blake ridge (Hornbach et al., 2008), or on the Cascadia (e.g. Ganguly et al., 2000; Hobro et al., 2005; He et al., 2007; Riedel, 2007) and Nankai (e.g. Martin et al., 2004; Bangs et al., 2010) margins, as well as combined seismic reflection/refraction experiments conducted in the North Sea (e.g. Westbrook et al., 2008). In our opinion, dense surveys are keys to more precise description of hydrate forming geological structures, and the formulation of a "petroleum type" model of hydrate emplacements.

In order to understand the details of BSR distribution and their relationships with local structures and observed geochemical anomalies, a set of closely spaced (250–500 m line-spacing) MCS data together with wide-angle data (recorded by OBS) were acquired over a 15 × 15 km wide area in the submarine orogenic wedge where rapid deposition of organic carbon-rich terrigenous sediments combined with strong dewatering (upward fluid flow) processes may provide a source for methane generation and motor for gas hydrate accumulation. This paper presents the analysis of this dense seismic data volume.

1.1. Geological setting

The island of Taiwan is located at the junction of the Ryukyu and Luzon island arcs along the western margin of the Philippine Sea. The orogen of Taiwan results from the collision of the Luzon volcanic arc with the passive China Continental Margin (CCM) since Pliocene time (Biq, 1972; Ho, 1986; Teng, 1990). The obliquity of the convergence, (307° N versus 350-10° trend of the collision zone, at a rate of about 7 cm/yr; Seno et al., 1993), induces a southward propagation of the collision (Suppe, 1987). South of Taiwan, along the Manila subduction zone, the sediments derived from both the Taiwan orogenic belt as well as the China Continental Margin deposit in the South China Sea and are subsequently accreted to Manila accretionary prism (Reed et al., 1992). This oceanic subduction evolves into an incipient collision north of 21°30′, as the subduction system encroaches on the northern continental slope of the South China Sea passive margin obliquely, the South China Sea basin closes, and the submarine accretionary wedge emerges to form the sub-aerial Taiwan orogen (Liu et al., 1998). The distinctive horst and graben structures of the Chinese continental shelf and the fold-and-thrust structures of the convergent domain are separated by a deformation front (Fig. 1) that extends NNW-ward from the Manila Trench across the foot of the continental slope and the Kaoping shelf, and connects to the frontal thrusts of the mountain belt of Taiwan (Liu et al., 2004). The structures east of the deformation front are dominated by en-echelon-arranged fold structures forming a curved belt that is convex toward the foreland, and which can be subdivided in three domains (Lin et al., 2008): the frontal segment, characterized by four series of west-vergent blind thrusts with gently folded limbs, followed by the central segment, characterized by west-vergent emergent and imbricate thrusts with tilted beds truncated at the hangingwalls, that culminate arcward with the "Good Weather Ridge (GWR)", and finally the upper slope domain, characterized by mud diapirs often buried by recent mud layers (Chuang, 2006).

In this paper, we focus on the fold-and-thrust unit located at the eastern edge of the central segment and south of the GWR, where an NNW–SSE elongated slope basin provides a peculiar setting for the deformation of the accretionary wedge, fluid and gas migration paths, and gas hydrate emplacements.

1.2. Dense seismic experiment

Our dense seismic reflection/refraction survey, with a total 775 km of profiling acquired in 2006, consists of 29 E–W profiles with 500-m line-spacing and 18 N–S profiles with up to 250-m line-spacing in the center. The MCS data were collected using a small air-gun array with a total volume of 580 in^3 and a 24-channel streamer of 300 m in length. The shot spacing is 25 m, while the receiver group interval is 12.5 m. Seismic data were processed with ProMAX (Landmark) and processing sequence comprises editing, mute (water column), surface consistent spiking predictive deconvolution, band-pass filtering (4–16–96–128 Hz), geometrical spreading
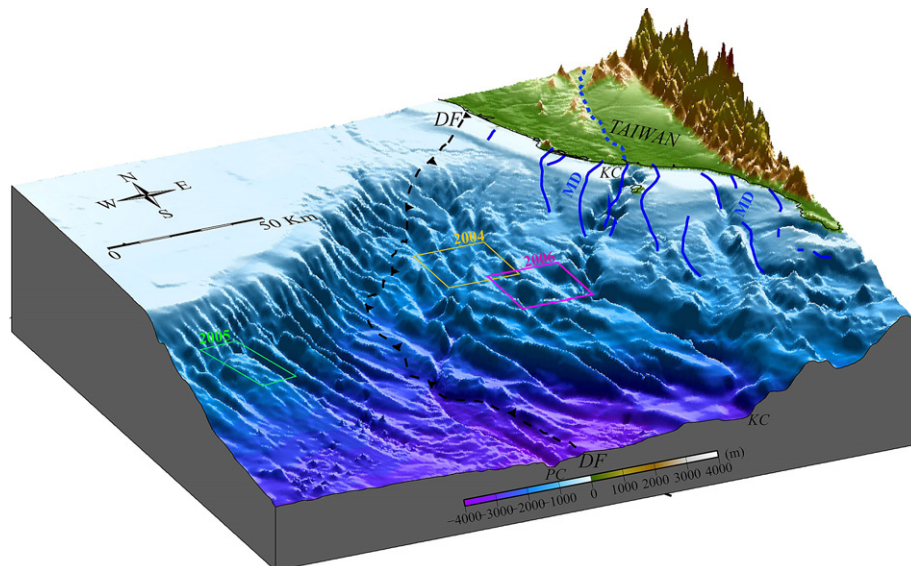

Figure 1. Shaded-hill bathymetric view of offshore southwestern Taiwan. The view is from the southwest, and the illumination is from NNE. Three boxes mark the survey areas of the adjacent pseudo-3D surveys conducted in 2004 (NW of GWR), 2005 (CCM), and 2006 (S of GWR; this study).
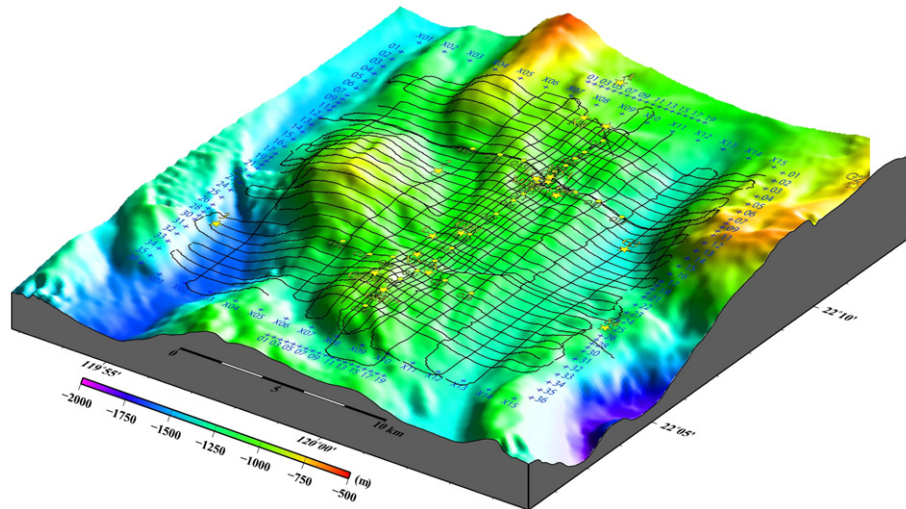
Figure 2. Shaded-hill bathymetric view of the survey. The view is from the southeast, and the illumination is from the west. The ship-tracks of the pseudo-3D survey, the OBS, and the coring sites, are draped on the bathymetry.

compensation, applying normal move-out followed by residual trim-static, stacking, and constant velocity (1500 m/s) FK time migration.

The seismic coverage is complemented by 12 previously acquired MCS profiles across this survey box in an NNE−SSW direction, thus we are able to make this data set into a pseudo 3-D (or 2.5-D in this study) seismic volume for analysis. During the MCS experiment, 30 Ocean Bottom Seismometers were deployed along 4 transects that are currently processed at the National Taiwan Ocean University. Finally, geochemical analyses performed on samples obtained from 21 coring sites are available, including one giant piston core acquired by N/V Marion Dufresnes (MD13; Fig. 2). Our point of view, in this particular study, is to focus on a narrow area with a dense multi-disciplinary approach in order to provide an accurate and primarily descriptive picture, although a complex one, of the structural setting and BSR character at the submarine accretionary wedge offshore southwestern Taiwan.

2. Data analysis

2.1. Structural analysis

The survey area (Fig. 2) is primarily composed of a 15 km broad anticlinal structure (the central ridge), in 600−1800 m water depths, bounded by N−S trending west-verging (arcward-dipping) thrusts to the east and west, and draped by a broad slope basin mainly composed of east-dipping (arcward-dipping) deposit (Fig. 3). From the bathymetric data, the slope gradient is lower than 10° in the survey area, except on the western limbs of the topographic ridges where it reaches 22°. Furthermore, the crest of the central ridge, bounded westward by the N−S running tributary of the Penghu Canyon, is oriented in an NNW−SSE direction, and offset westward by about 2 km from its northern (GWR) and southern N−S trending bathymetric extension. In the center of the slope basin, the bathymetry presents a gentle relief rising at-most 100 m that lies and extends across the entire survey area in an N−S direction. Then 2.5 km eastward, a second more gentle ridge is observed on the bathymetric map as a less than 50 m high relief: it is however accompanied by little deformation of the slope basin sediment at depth (Fig. 3).

The anticlinal system is bounded on both east and western sides by continuous N−S oriented and west-verging thrusts: at its east edge the frontal thrust is clearly imaged on both the bathymetric and seismic data over the entire survey area and marks the boundary between the middle and upper slope domains; at its western edge the frontal thrust outcrops along the N−S running tributary of the Penghu Canyon, but is followed eastward by a complex system of oblique ramps accompanied by duplexes (Fig. 3). Thus in the northern part, the central ridge is composed of R1, a 4 km wide anticlinal structure emerging just east of the frontal thrust, followed by the anticlinal GWR bounded westward by a system of oblique ramps, and in turn overridden by R3 ridge eastward (Fig. 3a). Southward, active thrusting of the GWR ceases and the GWR progressively disappears while buried under the sediment deposited in the slope basin. In the center of the survey area, the central ridge is composed of a duplex of R1 (buried) and R2 (Fig. 3b). Emergent thrusts have upthrown the hangingwall strata of R2, and bedding dips monotonously arcward and is often truncated at the hangingwall. Then in the southern part of the survey area, another system of oblique ramps is observed, and a fate similar to the southern termination of the GWR awaits R2: R1 broadens while R2 is progressively buried and disappears southward, while overridden eastward by R3 (Fig. 3c). As a matter of fact, the GWR, R2, R1 ridge system associated with the western thrusts, arranged in a relay pattern, whereas one fault dies out along strike and its displacement is transferred to a neighboring fault, is observed in most of the central domain of SW Taiwan (Lin et al., 2008): the emergent thrusts occur where the vertical faulting displacements are greatest. They gradually become blind thrusts in either lateral tip of the ridges, as the vertical faulting offsets decrease along strike and both the folds and related faults terminate, resulting in plunging anticlines: a pattern coined by Lin a relay fault array (Lin et al., 2008).

In this respect however, the central fold R3 is atypical: it extends across the entire survey area in an N−S direction and connects to similar structures that can be traced NNE-ward to the Taiwan coastline. Furthermore, R3 is accompanied by bright reflections and numerous diffractions along the outer-rims of the fold on the seismic profiles (Fig. 3). Also, R3 fold assumes a symmetric shape over most of the survey area, where it is bounded to the west by a minor east-verging back-thrust. Only at the northern and southern edges of this area, where R3 actively overrides the GWR and R1 respectively, does the R3 fold evolve toward an asymmetric anticline bounded to the west by a west-verging active thrust.
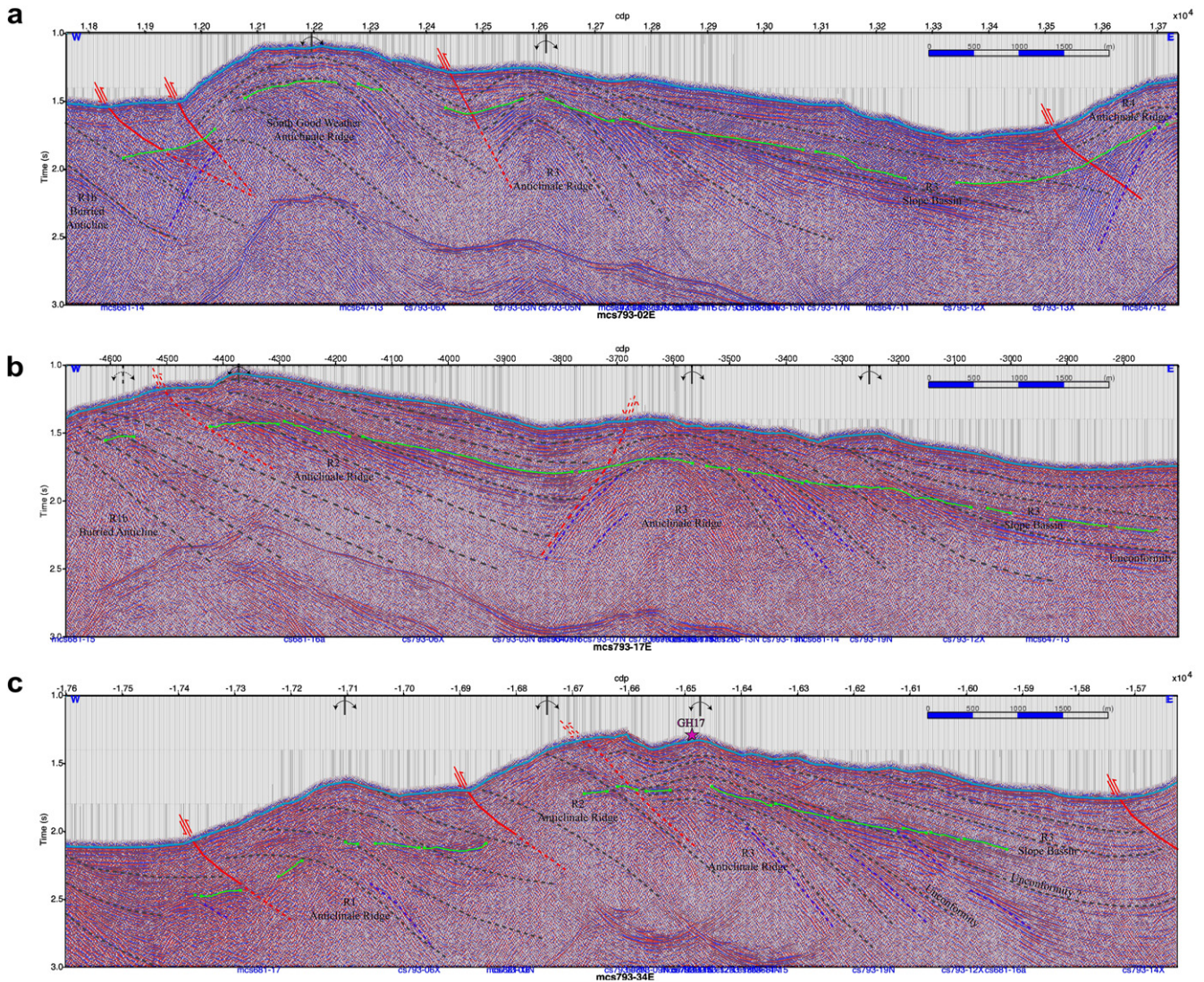
Figure 3. MCS793-02 (a), MCS793-17 (b), and MCS793-34 (c), located to the north, center, and south of the survey area, respectively. The seismic sections are FK time-migrated, and overlain by the structural interpretation and identified BSR. The vertical exaggeration at seafloor is 3.

We therefore propose that the atypical structures of R3 result from a gravitational control (buoyancy) and strain weakening, due to strong fluid advection. This ridge might in fact represent the early stage of formation of the mature diapiric ridges observed on the Kaoping shelf (Fig. 1; Chuang, 2006).

The structural dips in the backlimbs of GWR, R2, and R1 are relatively constant, presenting sub-parallel bedding and little sedimentation, with dips decreasing southward between arrays owing perhaps to the southward weakening of the collisional stress due to the NE trend of the SCS continental shelf: structural dips in R3 increase with depth, indicating continued relative uplift during sedimentation, at sedimentation rates that increase southward. The syntectonic surfaces of growth strata of the slope basin are fanning outwards, with beds progressively thinning toward the fold crest and decreasing in dip upwards (Fig. 3), indicating that uplift rates are slower than that of sediment accumulation (Burbank and Verges, 1994). Furthermore, the fanning growth strata of the slope basin are bounded at their top by an onlapping arcward-dipping unconformable sequence, most pronounced in the southern part of the study area (Fig. 3c), and at rather variable depths across the survey area but generally increasing southward.

The unconformity's undulations suggest that a period of episodic uplift activity of the R3 ridge, accompanied by laterally variable rates, was followed until present times by a period dominated by intra slope basin deposition. Seismic imaging in intra slope basin is relatively poor, and no channel incisions can be identified on the seismic profiles.

Finally, Figure 4 presents the survey layout and our structural interpretation. Figure 5 summarizes the 3D structural features in the survey area as shown by a series E–W and N–S line drawings.

2.2. Core geochemistry

In the study area, sediment cores were recovered from 23 coring sites (see Figure 4 for locations). Seafloor sediments consist essentially of fine-grained mud, averaging 95% of the total sediments. Major mineral components include illite (60%), chlorite (29%), smectite (9%), kaolinite, calcite, quartz, and feldspar: sediment similar to the source rock on-land Taiwan is observed (at site MD13; Jiang et al., 2006). Porosity varies from 14 to 61%, but a vast majority of cores presents porosities of 56%, and bulk density from 1.8 to 2.2 g/cm^3. Grey mud is found at sites G3 and GH16, soft
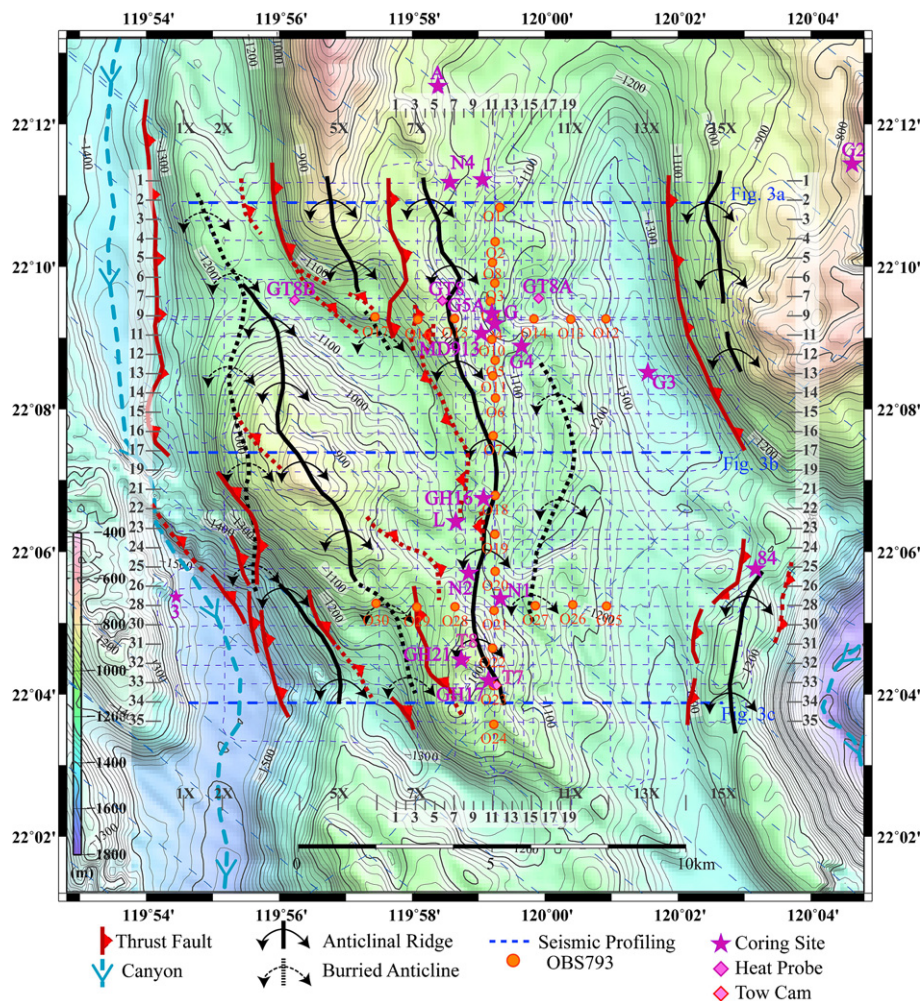
Figure 4. Shaded-hill bathymetric map and structural features of the survey area. Thirty-five E–W profiles with 500 m line-spacing, and 16 N–S profiles with up to 250 m line-spacing, together with 2 OBS transects, were collected in 2006. Two tow-cam surveys, 4 heat-probe measurements, and 21 sedimentary cores have also been acquired in our study area. Blind thrusts and poorly imaged faults are marked with dash lines, faults that breach to the seafloor or show significant offset are marked with continuous lines.

mud with shells at sites N4 and G4, sandy mud at sites N2 and G5a, and grey hard mud at sites N1 and GH1 (T7), while other sites present mud. The total organic carbon content (TOC) is about 0.65%. Na and Cl variations are generally less than 10%. Methane concentration in the bottom water range from 0.2 to 46 μL/L. Methane is probably of biogenic origin ($\delta C^{13} = -55‰$ carbon isotopic ratio, $\delta O^{18} = 5$ analyzed at site GH16; Yang et al., 2006). Methane concentration in the core sediments at stations G3, G5a, MD13 and GH16 increases with depths, while rather randomly at other sites, with maximal values (in ml/L) of 0.5 at N2 and N4, 1 at N1 and G3, 10 at G5a and MD13 (Chuang et al., 2006). Total sulfate depletion is generally observed through the bottom of the cores, and as shallow as 2.75 m at site GH16. The chemical and isotopic characteristics of pore water separated from piston cores suggest a strong influence of organic matter degradation during sediment diagenesis and support only minor degree of gas hydrate dissolution of formation at shallow depths. However, core breakage and gas fissures due to gas expansion have also been observed (Jiang et al., 2006).

Dissolved sulfide and high chloride concentrations are observed, but dissolved sulfide occurs before total sulfate depletion at several cores (Lin et al., 2006). Framboids and irregular aggregates of fine-grained pyrite with some overgrowth are observed at N4 and GH16. At site G5a, magnetite exists in the top, while pyrite exists in the

lower part of G5 (Huang et al., 2006). Magnetite is formed from detritus while gregite and pyrite were formed after sediment deposits, suggesting long term gas seepage.

2.3. BSR analysis

We mapped the BSR distribution, computed the BSR sub-bottom depths, and associated geothermal gradient values. We digitized all BSRs identified from our seismic data volume. Figure 6a presents the BSR distribution in the survey box, where the color scale indicates the BSR sub-bottom depth. Given the low fold and short offsets (377.5 m maximum offset) of this data set, semblance stacking velocity analysis is unreliable, and we performed the normal move-out and the time to depth conversions with a unique velocity versus sub-bottom depth function, based on Hamilton's geoacoustic model (Hamilton, 1980) which was created from drill-holes from 20 areas of terrigenous sediments in the North Pacific and adjacent areas, and given by: $V_{avg}(t) = 1511 + 1041 \times t - 372 \times t^2$, where t is the one-way travel time below seafloor. The conversion to sub-bottom depth is then given as $z(t) = t \times V_{avg}(t)$. This relationship was used in previous BSR distribution studies offshore southern Taiwan (Chi et al., 1998; Shyu et al., 2006; Schnurle and Liu, 2009), and is in good accordance with the sub-bottom velocities obtained from the inversion
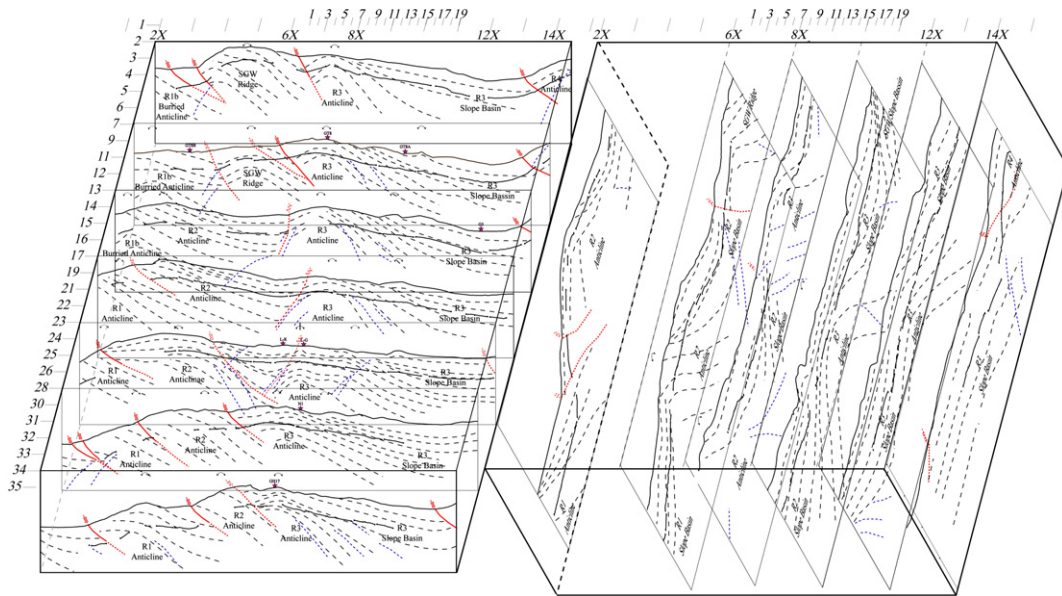
Figure 5. Structural features along a series of E–W and N–S profiles arranged as a 3D chart. The GWR, R2, R1 relay-ridge system associated with the western ramps and thrusts produces plunging anticlines characterized by considerable N–S shortening in the forelimbs of GWR and R2. In the anticlinal backlimbs, the growth strata are rapidly uplifted at the R3 fold, while accompanied by significant sedimentation in the east.

of the OBS deployed in the adjacent 2004 OBS experiments (Cheng et al., 2006; Schnurle et al., 2006), as well as the OBS deployed in this area (Wang et al., 2010). As a matter of fact, along the N–S OBS profile (Fig. 4), low P-wave velocity of 1.4–1.72 km/s and relatively high Poisson's ratio of 0.47–0.48 below the BSR are attributed to 30–120 m thick free gas bearing sediment. Furthermore, Wang et al. delineate two areas of high P-wave velocity of 1.87–2.04 km/s and relatively low Poisson's ratio of 0.445–0.455, with a thickness of about 100–150 m above the BSR, with the highest potential hydrate saturation: at the crest of R3 in the center of the study area below OBS 4–6, and southern tip of R3 below OBS 23. Peak gas saturation reaching 0.75–1.1% in a homogeneous distribution and 3–4% in a patchy distribution is proposed 1.5 km northward beneath these 2 areas, below OBS 5–9 and OBS 21 (Wang et al., 2010).

Also, assuming the BSR marks the base of the hydrate stability field, for a given depth of the BSR the temperature at the BSR can be calculated from an empirical relationship for hydrate stability, and an estimate of the local geothermal gradient can be obtained (e.g. Yamano et al., 1982; Fig. 6b). In this study, we assume for the geothermal gradient calculation a simple and conservative conductive thermal model, with a constant temperature of 4.25 °C at the seafloor, a constant 1 W/°C/m^2 conductivity above the BSR, and hydrate forming in hydrostatic pressure conditions from pure methane gas and brine at 19 ppm chlorinity, and a dissociation temperature regression formula according to Tishchenko et al. (2005).

The BSR is observed over 520 km, i.e. 67% of profiling. The BSR is densely distributed throughout most parts of the slope basin. As the BSR becomes parallel to the sedimentary layers, its identification becomes difficult: we are thus unable to map the BSR in the southeastern corner of R2 slope basin. BSR identification is also difficult in the 2 oblique ramp systems, where seismic imaging is relatively poor due to the structural complexity. Finally, it is surprising that few BSRs are observed at the crests of R1 and R2. The estimated geothermal gradient ranges from 40 to 70 °C/km. In the slope basin values are near 45–55 °C/km, but are elevated to 55–65 °C/km along the slope ridge R3, while reaching 70 °C/km at the southern tip of the GWR (Fig. 6b). These values are in good

agreement with a previously published geothermal gradient of 55 °C/km, interpolated at our study area and derived from a set thermal heat-probe measurements offshore southwestern Taiwan (Shyu et al., 2006). Furthermore thermal heat-probe measurements have been collected at four sites of our study area, and the bottom water temperature (T_0 in °C), thermal conductivity (K in W/°C/m^2), and geothermal gradient before sedimentation correction (G in °C/km) are: $714 - T_0 = 4.462$, $K = 0.96$, $G = 3$; $T6 - T_0 = 4.287$, $G = 30$; $GT8 - T_0 = 4.090$, $K = 1.46$; $GT8A - T_0 = 3.705$, $K = 1.006$, $G = 37$; $GT8B - T_0 = 3.492$, $K = 1.59$. Indication of hydrate dissociation was found at sites 714 and GT8A, while the high thermal conductivity at sites GT8 and GT8B was attributed to wetter sediments (containing more sea water – Shyu, personal communication; Shyu et al., 2006). The thermal equilibrium between deep seated "flat" isotherms alimented by radiogenic heat and water bottom cool temperatures is particularly driven by topography (e.g. He et al., 2007): bathymetric highs coincide with low geothermal gradient, most pronounced at the anticinal ridges, while erosional channels along the Penghu Canyon (and along the western limbs of anticlines) are loci of high gradients. The geothermal gradient estimates from BSR sub-bottom depth are also sensitive to the thermal conductivity: the variations (45–65 °C/km) in this area could well result from 18% variations in the conductivity, due for instance to weaker/higher water content along the homocline R2 and the central ridge R3, respectively, rather than to local heatflow variations. Finally, our estimates are less sensitive to the time to depth conversion: when doubling the linear velocity parameter in Hamilton's formula ($v1 = 2082$), both BSR depth and temperature increase, and the estimated geothermal gradient decreases on average by 5 °C/km, a variation far below those observed in our study area.

Fluid and gas flows across the BSR and into the gas hydrate stability zone are critical to the accumulation of gas hydrate. Faults are known to act as major conduits; fractures are believed to provide paths for considerable flux, but these are often sub-vertical, and fracturing is difficult to measure with remote sensing techniques, e.g. seismic. Fluid and gas flux guided along the sedimentary bedding, resulting from horizons with variable permeability, is
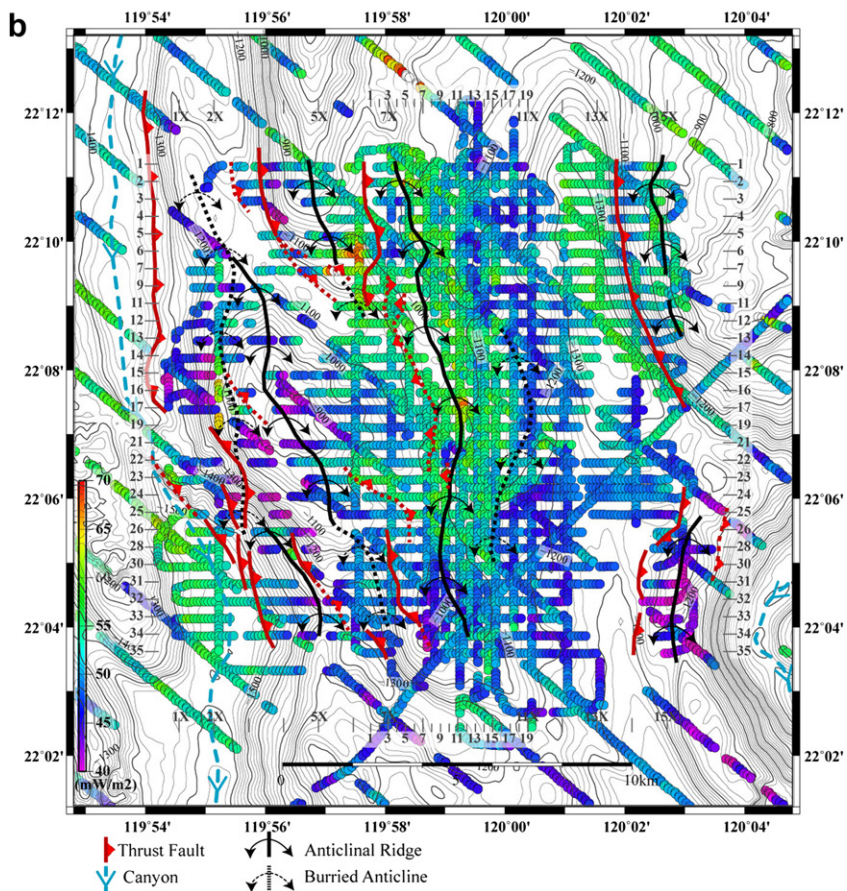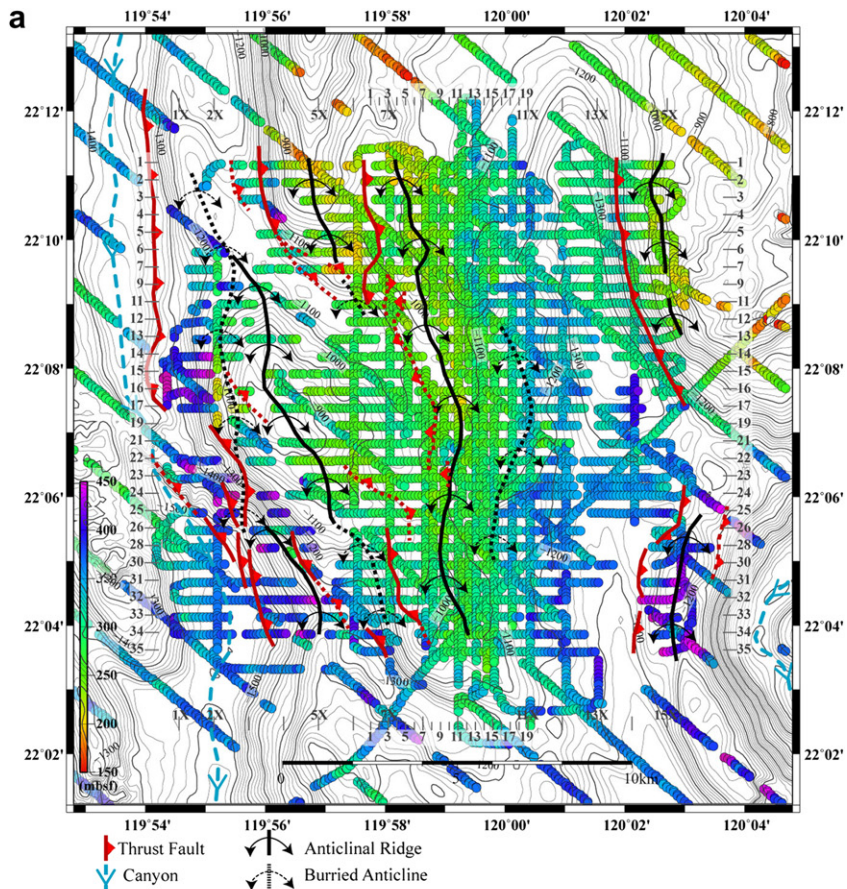
Figure 6. (a) BSR sub-bottom depth and (b) derived geothermal gradient. Local geothermal gradient is low along the western limbs and crest of the anticlines ranging from 40 to 50 °C/km, increase toward 50–60 °C/km in the slope basin and 55–65 °C/km along R3, and reach maximal values of 70 °C/km at the southern tip of GWR.

likely to add a significant component to the total flux, particularly when considering lateral migration paths. This component can be estimated as stratigraphic dips can be established from the seismic volume. Considering that advective fluid flow exceeds diffusive flow in the tectonically dewatering submarine orogenic wedge, and that fluid paths are following the bedding, we therefore propose that the intensity of the fluid flow is controlled by the dip of the bedding. The bedding-guided fluid and gas migration path, that

enters across the BSR into the hydrate stability field, is thus proportional to the dot product of the structural dip (Fig. 7a) and the normal to the BSR surfaces (Fig. 7b), and is likely to follow the patterns in Figure 7c.

We have calculated local dips and strikes of the BSR and of the statigraphic horizon that cross cuts the BSR at the intersections of any 2 seismic profiles. In the presence of high angle faults, we have considered the fault-plans instead of sedimentary horizons
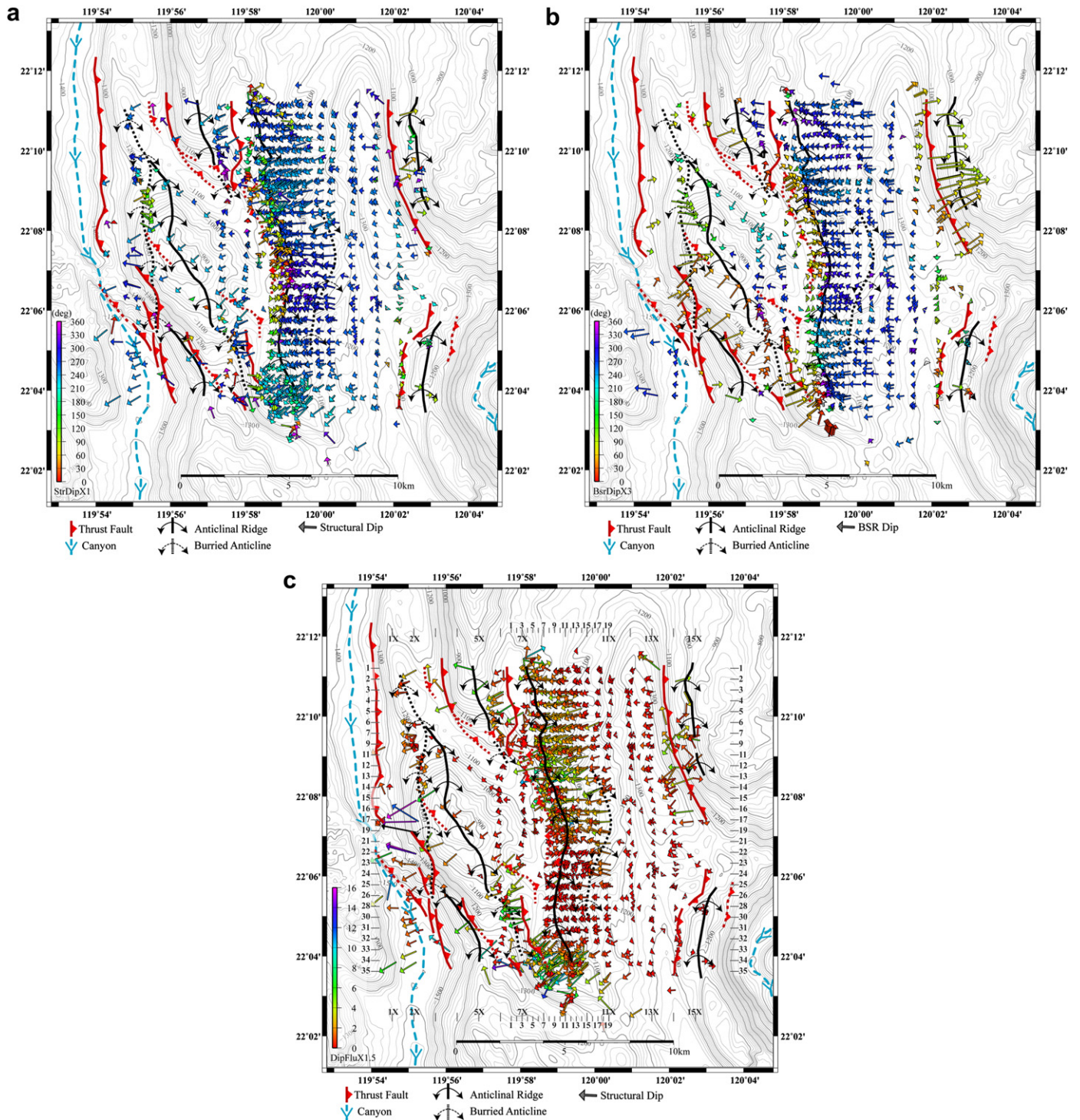

Figure 7. Estimated fluid and gas migration path and intensity; the arrow lengths are proportional to the sine of the angles. (a) Stratigraphic dip of the sedimentary strata just below the BSR (colored according to azimuth, 0.75 arrow length exaggeration); (b) dip of the BSR (colored according to azimuth, 2 arrow length exaggeration); (c) bedding-guided fluid and gas migration flux (colored according to intensity, no arrow length exaggeration).

as acting conduit. Figure 7 shows the up-dip directions of the sedimentary strata (or fault) at BSR (Fig. 7a), and the up-dip direction of the BSR (Fig. 7b) where the arrow length is proportional to the sine of the dip. The BSR depth has been gridded to a continuous surface from which dips were extracted at seismic intersections. Since structural dips were estimated for each seismic line, intersections are processed twice: when seismic imaging is poor, our interpretation of the bedding may differ and 2 conflicting dips are mapped (Fig. 7a), giving a rough estimate of the reliability of this method. Such conflicting interpretations occur particularly in bedding characterized by dips greater than 30°, where the MCS acquired with a short streamer results in poor imaging, and further depends on the obliquity of the seismic profile and the bedding (out-of-plain events).

The dominant trend of shortening in the survey area is E–W (Fig. 7a); however, N–S shortening also affects the western half of the survey area, with stratigraphic dips verging SW in the hangingwall of GWR, R2, and R1, suggesting a main direction of shortening almost perpendicular to the plate to plate converge at these locations, in sharp contrast to the plate convergence parallel shortening observed in anticlines located NW of GWR (Schnürle and Liu, 2009). Stratigraphic dips as high as 35°, with an SW strike, characterize the lateral thrust systems at the southern crest and forelimb of the GWR and R2 plunging anticlines. Dips in excess

of 20°, with an E–W strike, are observed on the eastern flanks of R3 fold in the northern half of the study area, but dropping to less than 15° in the southern half. Bedding in the western flanks of R3 strikes NW at the center of the survey area, fanning toward the SW when approaching the lateral ramp systems. High amplitude bedding at angles up to 45–50° marks the northern edge of the R3 diapir, while dips are either too high or seismic continuity too poor inside the diapir to achieve seismic imaging.

The intensity of the estimated bedding-guided fluid and gas flux into the hydrate zone is weaker than 2 in the slope basin, nears 10 in the forelimb and crest of the ridges (GWR, southern portions of R2 and R3), and reaches a maximum of 16 at the fault plain of the frontal thrust of R1 (Fig. 7c). Along the R3 ridge, the flux is estimated around 2 in the GWR–R3 duplex to the NW, then increasing to 5–10 in the SE termination of the GWR, abruptly dropping to less than 1 in the central part (slope basin) as bedding and BSR become sub-parallel, before it peaks again at 5–10 in the R2–R3 duplex to the SE.

3. Discussion and conclusive remarks

This survey area is characterized by a complex structural setting, accompanied by rapid lateral variations in seismic character. Figure 8 summarizes the BSR and structural features in our study area: we have identified the areas where the BSR is observed, those
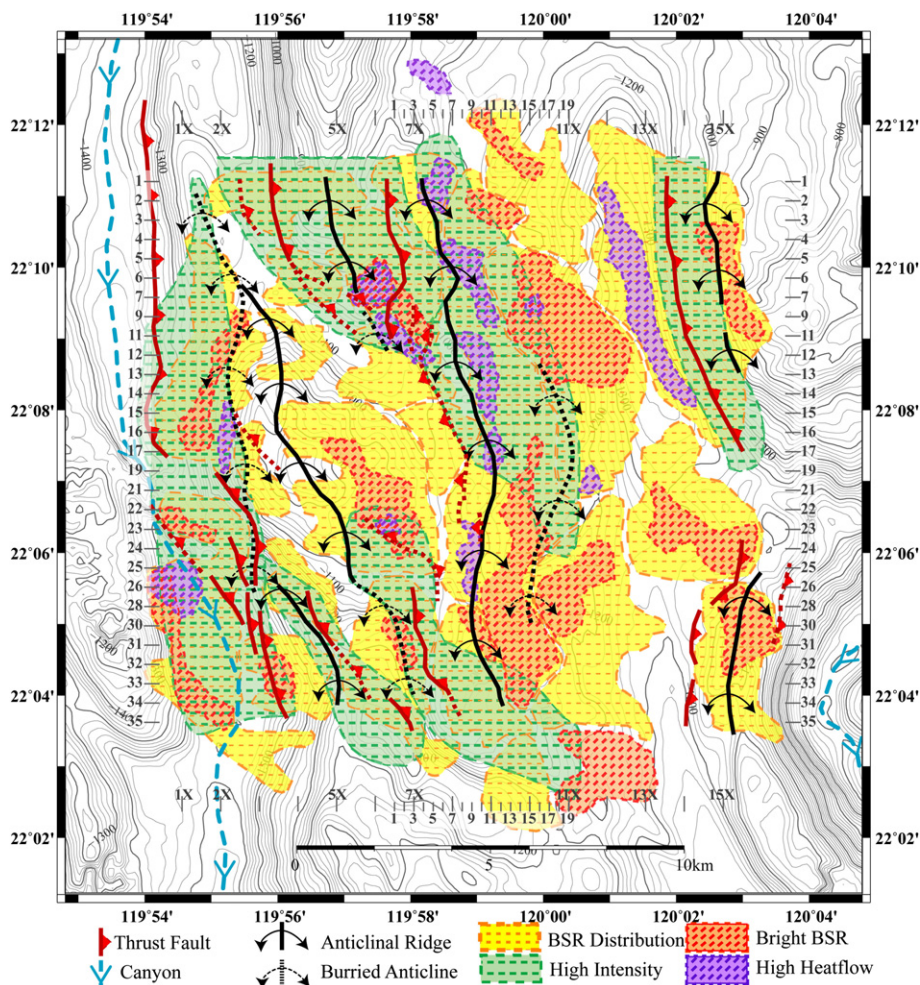

Figure 8. Distribution of BSR character and structural features. The areas where the BSR is observed are marked in yellow. The areas where the BSR is bright and corresponding to BSR seismic amplitude in excess of 60% of the BSR maximal observed amplitude are marked in red. The areas corresponding to high (exceeding 55 °C/km) estimated geothermal gradient are marked in violet. Where MCS intersections are numerous, regions where flux intensity exceeds 3 are interpreted as high bedding-guided flux areas and are marked in green. (For interpretation of the references to color in this figure legend, the reader is referred to the web version of this article.)

where the BSR is bright (amplitude in excess of 60% of the BSR maximal observed amplitude), the areas corresponding to high (exceeding 55 °C/km) estimated geothermal gradient, and those of high bedding-guided flux (intensity exceeding 3). These results suggest similar conclusion to those gained from the analysis of the 2004 pseudo-3D survey conducted NW of the GWR (Schnurle and Liu, 2009):

1) On one hand, active shortening results in tectonic uplift accompanied by downward migration of the BSR, and in high angle stratigraphic dips that constitute favorable migration paths for the fluid and gas transport into the gas hydrate stability zone. Weak or no BSR is observed at the crest of R2, suggesting active uplift and thickening of the hydrate stability zone. On the other hand, the rapid sedimentation in the slope basin opposes this fluid flux, and results in upward migration of the BSR and hydrate decomposition.

2) The maximum fluid and gas transport across BSR should occur below the crest of anticlines. Strata that are sub-parallel to BSR, i.e. in the slope basin, should allow the lowest degree of transport across the BSR into the hydrate stability zone, i.e. weak intensity.

3) Low velocity anomalies derived from pre-stack depth migration velocity analysis and OBS tomographic inversions along the EW9509-33 reflection/refraction experiment, running E–W along the northern boundary of our dense survey, are observed below the BSR (Schnurle et al., 2004). Similar observations were made at the 2004 MCS/OBS experiment (Cheng et al., 2006; Schnurle et al., 2006) and in this survey area (Wang et al., 2010). Therefore, the bright reflections observed below BSR in the eastern portion of R2 and R3 (Fig. 3) can be attributed to the presence of free gas in the pore-space.

4) These areas of particularly bright BSR are systematically adjacent to areas of high flux intensity: areas of bright BSR are located against the eastern edges of areas of high intensity, both in the slope basin and R2 anticline. At such lesser dips, local changes of temperatures through warmer fluid transport would result in gas release due either to a decrease of solubility or the shallowing of the BSR, and the occurrence of particularly bright BSR. In the slope basin for instance, strong sedimentation leads to upward migration of the BSR, resulting in the dissociation of hydrates at the base of the stability zone; the weak fluid and gas flux where strata lie sub-parallel to the BSR prevents the free gas from entering the stability zone, and thus producing the bright spots on the seismic profiles. Therefore, the presence of free gas on seismic profiles does not generally correspond to areas favorable to gas hydrate emplacements.

5) Along the N–S OBS profile, our estimated flux intensity is rather homogeneous and lower than 5, except for 2 distinctive areas each about 1 km wide below OBS 5 and OBS 24, where intensity exceeds 8 and 12, respectively (Fig. 7c). These are located within the 2 regions where up to 25% saturation is inferred by Wang et al. (2010). Also peak gas saturation proposed by Wang et al. (2010) coincides with the peak structural dips, up to 30° between OBS 5 and 9, and with high structural dips of 15° at OBS 21. Also, the highest dissolved methane values in the piston cores acquired in the survey area are located in the vicinity of OBS 5: 10 ml/L at G5a and MD13 (Chuang et al., 2006).

6) The symmetric shape of R3 fold in the central part, accompanied by back-thrusting, suggests that the E–W shortening in R3 is accompanied by vertical stress: the sediment is likely weaker and more buoyant in R3 when compared to the surrounding slope basin sediment. Furthermore, areas of high geothermal gradient often mark the flanks of R3, in sharp contrast with the expected low geothermal gradients generally associated with bathymetric ridges. The bright reflections and strong diffractions on the seismic profiles could also indicate high pore–fluid activity, and perhaps hydro-fracturing. When nearing the sub-surface, the fluid channels are forced into more narrow conduits as several mud-volcanoes are observed. Therefore, this ridge might represent the early stage of formation of the mature diapiric ridges observed on the Kaoping shelf.

References

Bangs, N., Hornbach, J.M., Moore, G.F., Park, J.O., 2010. Massive methane release triggered by seafloor erosion offshore southwestern Japan. Geology 38, 1019–1022. doi:10.1130/G31491.1.

Biq, C.C., 1972. Dual-trench structure in the Taiwan–Luzon region. Proceeding of the Geological Society of China 15, 65–75.

Bünz, S., Mienert, J., Berndt, C., 2003. Geological controls on the Storegga gas-hydrate system of the mid-Norwegian continental margin. Earth and Planetary Science Letters 209, 291–307. doi:10.1016/S0012-821X(03)00097-9.

Burbank, D.W., Verges, J., 1994. Reconstruction of topography and related depositional systems during active thrusting. Journal of Geophysical Research 99, 20281–20297.

Chuang, H.-J., 2006. Distribution and Structural Relationships of Mud Diapirs Offshore Southwestern Taiwan. MSc. thesis, Institute of Oceanography, National Taiwan University. 113 pp.

Chuang, P.C., Yang, T., Lin, F.S., Lee, H.F., Lan, T.F., Hong, W.L., Liu, C.S., Chen, J.C., Wang, Y., 2006. Extremely high methane concentration in bottom water and cored sediments from offshore southwestern Taiwan. Terrestrial Atmospheric and Oceanic Sciences 17, 903–920.

Cheng, W.-B., Lee, S.-C., Liu, C.-S., Schnurle, P., Lin, S.-S., Tsai, H.-R., 2006. Velocity structures in marine sediments with gas hydrate reflectors in offshore SW Taiwan: from OBS data tomography. Terrestrial Atmospheric and Oceanic Sciences 17 (4), 739–756.

Chi, W.C., Reed, D.L., Liu, C.S., Lunberg, N., 1998. Distribution of the bottom simulating reflector in the offshore Taiwan collision zone. Terrestrial Atmospheric and Oceanic Sciences 9, 779–793.

Dai, J., Snyder, F., Gillespie, D., Koesoemadinata, A., Dutta, N., 2008. Exploration for gas hydrates in the deepwater, northern Gulf of Mexico: Part I. A seismic approach based on geologic model, inversion, and rock physics principles. Marine and Petroleum Geology 25, 830–844. doi:10.1016/j.marpetgeo.2008.02.006.

Ganguly, N., Spence, G.D., Chapman, N.R., Hyndman, R.D., 2000. Heat flow variations from bottom simulating reflectors on the Cascadia margin. Marine Geology 164, 53–68.

Hamilton, E.L., 1980. Geoacoustic modeling of the sea-floor. Journal of the Acoustic Society of America 68, 1313–1340.

He, T., Spence, G.D., Riedel, M., Hyndman, R.D., Chapman, N.R., 2007. Fluid flow and origin of a carbonate mound offshore Vancouver Island: seismic and heat flow constraints. Marine Geology 239, 83–98. doi:10.1016/j.margeo.2007.01.002.

Ho, C.-S., 1986. A synthesis of the geologic evolution of Taiwan. Tectonophysics 125, 1–26.

Hobro, J.W.D., Minshull, T.A., Singh, S.C., Chand, S., 2005. A three-dimensional seismic tomographic study of the gas hydrate stability zone, offshore Vancouver Island. Journal of Geophysical Research 110, B09102. doi:10.1029/2004JB003477.

Hornbach, M.J., Saffer, D.M., Holbrook, W.S., Van Avendonk, H.J.A., Gorman, A.R., 2008. Three-dimensional seismic imaging of the Blake Ridge methane hydrate province: evidence for large, concentrated zones of gas hydrate and morphologically driven advection. Journal of Geophysical Research 113, B07101. doi:10.1029/2007JB005392.

Huang, C.Y., Chien, C.W., Zhao, M., Li, H.C., Iizuka, Y., 2006. Geological study of active cold seeps in the syn-collision accretionary prism Kaoping slope off SW Taiwan. Terrestrial Atmospheric and Oceanic Sciences 17, 679–702.

Hustoft, S., Mienert, J., Bünz, S., Nouzé, H., 2007. High-resolution 3D-seismic data indicate focussed fluid migration pathways above polygonal fault systems of

the mid-Norwegian margin. Marine Geology 245, 89–106. doi:10.1016/j.margeo.2007.07.004.

Jiang, W.T., Chen, J.C., Huang, B.J., Chen, C.J., Lee, Y.T., Huang, P.R., Lung, C.C., Huang, S.W., 2006. Mineralogy and physical properties of cored sediments from the gas hydrate potential area of offshore southwestern Taiwan. Terrestrial Atmospheric and Oceanic Sciences 17, 981–1007.

Lin, A.T.-S., Liu, C.-S., Lin, C.-C., Schnurle, P., Chen, G.-Y., Liao, W.-Z., Teng, L.-S., Chuang, H.-J., Wu, M.-S., 2008. Tectonic features associated with the overriding of an accretionary wedge on top of a rifted continental margin: an example from Taiwan. Marine Geology 255, 186–203.

Lin, C.-C., Lin, A.T.-S., Liu, C.-S., Liao, W.-Z., Schnurle, P., 2009. Geological controls on BSR occurrences in the incipient arc–continent collision zone off southwest Taiwan. Marine and Petroleum Geology 26 (7), 1118–1131.

Lin, S., Hsieh, W.C., Lim, Y.C., Yang, T.F., Liu, C.S., Wang, Y., 2006. Methane migration and its influence on sulfate reduction in the Good Weather Ridge region, South China Sea continental margin sediments. Terrestrial Atmospheric and Oceanic Sciences 17, 883–902.

Liu, C.S., Huang, I.L., Teng, L.S., 1997. Structural features off southwestern Taiwan. Marine Geology 137, 305–319.

Liu, C.S., Liu, S.Y., Lallemand, S.E., Lunberg, N., Reed, D.L., 1998. Digital elevation model offshore Taiwan and its tectonic implications. Terrestrial Atmospheric and Oceanic Sciences 9, 705–738.

Liu, C.-S., Deffontaines, B., Lu, C.-Y., Lallemand, S., 2004. Deformation patterns of an accretionary wedge in the transition zone from subduction to collision offshore southwestern Taiwan. Marine Geophysical Research 25, 123–137.

Liu, C.-S., Schnürle, P., Wang, Y., Chung, S.-H., Chen, S.-C., Hsiuan, T.-H., 2006. Distribution and characters of gas hydrate offshore of southwestern Taiwan. Terrestrial Atmospheric and Oceanic Sciences 17, 615–644.

Martin, V., Henry, P., Nouzé, H., Noble, M., Ashi, J., Pascal, G., 2004. Erosion and sedimentation as processes controlling the BSR-derived heat flow on the Eastern Nankai margin. Earth and Planetary Science Letters 222, 131–144. doi:10.1016/j.epsl.2004.02.020.

Nagakubo, S., Kobayashi, T., Fujii, T., Inamori, T., 2007. Fusion of 3D seismic exploration and seafloor geochemical survey for methane hydrate exploration. Exploration Geophysics 38 (1), 37–43. doi:10.1071/EG07005.

Reed, D.L., Lundberg, N., Liu, C.-S., Kuo, B.-Y., 1992. Structural relations along the margins of the offshore Taiwan accretionary wedge: implications for accretion and crustal kinematics. Acta Geologica Taiwanica 30, 105–122.

Riedel, M., 2007. 4D seismic time-lapse monitoring of an active cold vent, northern Cascadia margin. Marine Geophysical Researches 28, 355–371. doi:10.1007/s11001-007-9037-2.

Seno, T., Stein, S., Gripp, A.E., 1993. A model for the motion of the Philippine Sea plate with NUVEL-1 and geological data. Journal of Geophysical Research 9, 17941–17948.

Schnurle, P., Hsiuan, T.-H., Liu, C.-S., 1999. Constraints on free gas and gas hydrate bearing sediments from multi-channel seismic data offshore southwestern Taiwan. Petroleum Geology of Taiwan 33, 21–42.

Schnurle, P., Liu, C.-S., Hsiuan, T.-H., Wang, T.-K., 2004. Characteristics of gas hydrate and free gas offshore southwestern Taiwan from a combined MCS/OBS data analysis. Marine Geophysical Research 25, 157–180.

Schnurle, P., Liu, C.-S., Lee, S.-C., 2006. Acoustic and shear-wave velocities in hydrate bearing sediments offshore southwestern Taiwan: tomography, converted waves analysis and reverse-time migration of OBS records. Terrestrial Atmospheric and Oceanic Sciences 17 (4), 757–779.

Schnurle, P., Liu, C.-S., 2009. Structural controls on the formation of BSR offshore southwestern Taiwan from a dense seismic reflection survey. In: Collet, T., Johnson, A., Knapp, C., Boswell, R. (Eds.), AAPG Memoir 89, Natural Gas Hydrate – Energy Resource Potential and Associated Geological Hazards, American Association of Petroleum Geologists, pp. 69–79.

Stockwell Jr., J.W., 1999. The CWP/SU: seismic Un*x package. Computers and Geosciences May.

Sultan, N., Voisset, M., Marsset, T., Vernant, A.M., Cauquil, E., Colliat, J.L., Curinier, V., 2007. Detection of free gas and gas hydrate based on 3D seismic data and cone penetration testing: an example from the Nigerian Continental slope. Marine Geology 240, 235–255. doi:10.1016/j.margeo.2007.02.012.

Suppe, J., 1987. The active Taiwan mountain belt. In: Schaer, J.P., Rodgers, J. (Eds.), Comparative Anatomy of Mountain Ranges. Princeton University Press, pp. 277–293.

Shyu, C.-T., Chen, Y.-J., Chiang, S.-T., Liu, C.-S., 2006. Heat flow measurements over bottom simulating reflectors, offshore southwestern Taiwan. Terrestrial Atmospheric and Oceanic Sciences 17, 845–969.

Teng, L.-S., 1990. Geotectonic evolution of the late Cenozoic arc–continent collision in Taiwan. Tectonophysics 183, 57–76.

Tishchenko, P., Hensen, C., Wallmann, K., Wong, C.-S., 2005. Calculation of the stability and solubility of methane hydrate in seawater. Chemical Geology 219, 37–52.

Wang, T.K., Yang, B.J., Deng, J.-M., Lee, C.-S., Liu, C.-S., 2010. Seismic imaging of gas hydrates in the northernmost South China sea. Marine Geophysical Research 31, 59–76. doi:10.1007/s11001-010-9096-7.

Wessel, P., Smith, W.H.F., 1995. New version of the generic mapping tools released. EOS Transactions, AGU, Supplement 76 (17), 29.

Westbrook, G.K., Chand, S., Rossi, G., Long, C., Bünz, S., Camerlenghi, A., Carcione, J.M., Dean, S., Foucher, J.-P., Flueh, E., Gei, D., Haacke, R.R., Madrussani, G., Mienert, J., Minshull, T.A., Nouzé, H., Peacock, S., Reston, T.J., Vanneste, M., Zillmer, M., 2008. Estimation of gas hydrate concentration from multi-component seismic data at sites on the continental margins of NW Svalbard and the Storegga region of Norway. Marine and Petroleum Geology 25, 744–758. doi:10.1016/j.marpetgeo.2008.02.003.

Yamano, M., Uyeda, S., Aoki, Y., Shipley, T.H., 1982. Estimates of heat flow derived from gas hydrates. Geology 10, 339–343.

Yang, T.-F., Chuang, P.-C., Lin, S., Chen, J.-C., Wang, Y., Chung, S.-H., 2006. Methane venting in gas hydrate potential area offshore of SW Taiwan: evidence of gas analysis of water column samples. Terrestrial Atmospheric and Oceanic Sciences 17 (4), 933–950.